

## Article

# The Influence of Vertical Seismic Acceleration on the Triggering of Landslides Constrained by Bedding Faults under an Inertial Frame Reference: The Case of the Daguangbao (DGB) Landslide

Guoping Xiang <sup>1</sup>, Tao Jiang <sup>1,\*</sup>, Qingwen Yang <sup>1,\*</sup>, Shenghua Cui <sup>1</sup> , Ling Zhu <sup>2</sup>, Yuhang He <sup>1</sup> and Huajin Li <sup>3</sup> 

<sup>1</sup> State Key Laboratory of Geohazard Prevention and Geoenvironment Protection, Chengdu University of Technology, Chengdu 610059, China; xiangguoping1989@163.com (G.X.); heyuhang1995@163.com (Y.H.)

<sup>2</sup> School of Geosciences and Info-Physics, Central South University, Changsha 410083, China; zhuling.cdut@gmail.com

<sup>3</sup> School of Architecture and Civil Engineering, Chengdu University, Chengdu 610106, China; lihuajin@cdu.edu.cn

\* Correspondence: jiang\_tao@stu.cdut.edu.cn (T.J.); yangqingwen20@cdut.edu.cn (Q.Y.)

**Abstract:** The Daguangbao (DGB) landslide was the largest landslide that was triggered by the 2008 Wenchuan earthquake with a magnitude of Ms8.0. The sliding surface of this landslide was constrained on a bedding fault 400 m below the ground surface. Seismic records show that the landslide suffered not only from strong horizontal but also vertical ground shaking that was almost equal to the horizontal component. In this study, to reveal the landslide triggering mechanism of the DGB landslide, this study ignores the steep dipping tension fracture section and the leading edge-locking section of the trailing edge of the DGB landslide, and the geological model of the large optical package landslide is generalized into a block model with the bottom controlled slip soft zone as the interface. Based on the improved Newmark method that considers vertical ground motion, the three-way seismic acceleration data and the shear strength parameter of the sliding surface being taken as a variable are used to calculate the cumulative permanent displacement of the slider. Then, by considering the cumulative permanent displacement ratio of vertical seismic acceleration or not and the cumulative permanent displacement ratio value considering the inertial force as the index, the response characteristics of the cumulative permanent displacement of the block-to-vertical ground motion and inertial forces were analyzed. The results show that both the horizontal inertial force and the vertical acceleration significantly increased the permanent displacement. The permanent displacement is 4.9 cm when considering the vertical acceleration, whereas it is only 2.0 cm without taking this into account. The contribution of vertical acceleration is significantly enlarged (87.8–90.7%) by the decreasing of the internal friction angle of the slide surface, while it is less influenced (5–27.4%) by the cohesion. Compared with the lower shear strength parameter of the sliding surface, the contributions of vertical acceleration and inertial force to the permanent displacement are more obvious when the shear strength parameter of the sliding surface is higher. When  $\phi > 18^\circ$ , the  $D/D^*$  is greater than 1, and the maximum  $D/D^*$  reaches 7. The fast accumulation event of permanent displacement is triggered in the concentration stage of the seismic energy release. In the DGB landslide area, 50% of the energy is released within 30–50 s, as indicated by the acceleration peaks recorded at the nearest seismic station, Qingping station. It is assumed that the DGB landslide may be triggered at 30–50 s due to half of the seismic energy being released during that time span.



**Citation:** Xiang, G.; Jiang, T.; Yang, Q.; Cui, S.; Zhu, L.; He, Y.; Li, H. The Influence of Vertical Seismic Acceleration on the Triggering of Landslides Constrained by Bedding Faults under an Inertial Frame Reference: The Case of the Daguangbao (DGB) Landslide. *Appl. Sci.* **2023**, *13*, 12911. <https://doi.org/10.3390/app132312911>

Academic Editor: Roberto Scarpa

Received: 15 September 2023

Revised: 12 November 2023

Accepted: 29 November 2023

Published: 2 December 2023



**Copyright:** © 2023 by the authors. Licensee MDPI, Basel, Switzerland. This article is an open access article distributed under the terms and conditions of the Creative Commons Attribution (CC BY) license (<https://creativecommons.org/licenses/by/4.0/>).

**Keywords:** DGB landslide; Newmark method; vertical acceleration; horizontal inertia force

## 1. Introduction

The seismic response study of landslides generally focuses on the study of the dynamic stability of landslides. The pseudo-static, numerical simulation, physical simulation,

Newmark method and probabilistic method are the main analytical methods used [1–10]. The principle of the pseudo-static method is simple, but it fails to consider the spectral characteristics of ground shaking and the effect of holding time [11,12]. Numerical and physical simulations can adopt the actual ground shaking to reproduce the dynamic response characteristics and damage process of slopes more realistically, but it is difficult to establish accurate models for slopes with complex geological conditions [13].

The Newmark method is a stability analysis method for dams that was proposed in 1965 [14], which is widely used because of its calculation simplicity. The method has undergone continuous refinement and improvement, from only considering the initial rigid block model to the fully coupled models [15], from only considering horizontal seismic acceleration to considering three-way seismic acceleration [16,17], and from only considering the constant shear strength parameters of the sliding surface to considering the dynamic parameters that are dependent on shear displacement [18]. Some scholars have tried to also consider the vertical seismic acceleration as a pseudo-static equivalent loading to participate in the solution of yield acceleration, but it caused great errors in the case of near-fault slopes with a large vertical component.

The vertical earthquake component's influence on the degree on seismic stability and slip deformation of geotechnical buildings has been discussed, and it is thought to have an important impact on the strength variations in structures [19,20]. Research has shown that the vertical component of an earthquake increases the nonlinear vertical displacement and the demand/capacity ratio in masonry structures [21,22]. It has been reported that the vertical component of an earthquake leads to a significant rise in the axial force in the central columns and even a collapse of the underground structures [23,24]. The variational mode decomposition technique is employed to show that the maximum displacement of elastomeric bearings subjected to a pulse-like horizontal ground motion is moderately amplified, on average, when the vertical excitation is also pulse-like [25]. The Daguangbao landslide was the largest landslide that was triggered by the Wenchuan earthquake and also a globally rare giant landslide. The earthquake records at the nearest Qingping seismograph station (51MZQ) show that the landslide area not only suffered strong horizontal seismic motion (0.824 g), but also received almost equal vertical seismic motion (0.8 g). However, only the horizontal ground motion is considered, and the vertical ground motion is ignored when using the Newmark method [26–28], so the improved Newmark method, which considers the direction of the vertical sliding surface, is used to calculate the permanent displacements of the Daguangbao (DGB) landslide. The hypothesis was that the vertical acceleration and horizontal inertia force increased the possibility of landslide instability. This can be due to the increase in the permanent displacement under vertical seismic acceleration, which can help to analyze the instability time of the Daguangbao landslide.

## 2. Materials and Methods

### 2.1. Study Area

In 2008, Wenchuan earthquake was the largest earthquake that had occurred in China since the Tangshan earthquake [29], the Lancang earthquake and the Gengma earthquake [30]. The strong ground shaking was felt 2000 km away in Shanghai, as well as in neighboring countries. In addition, the earthquake triggered a large number of landslides (6000–100,000 landslides were registered in an area of about 44,000 km<sup>2</sup>).

The DGB landslide, with a volume of  $1.2 \times 10^9$  m<sup>3</sup>, changed the topography of about 7.2 km<sup>2</sup> in the area, and the maximum length of the landslide area was 4.6 km. The profile shows the mass loss part, junction part and mobility part. The mobility mass was driven to be thrust on the slope on the other side of the valley with a height of 500 m. The landslide initiated along a bedding fault (Figure 1) [31,32]. The exposed rocks of the mass loss part and mobility part is main Carbonate rock and sandstone, and its lithology distribution has a good hierarchy, the west-to-east lithology is  $Tf \rightarrow P \rightarrow Ds \rightarrow Zd$  and the geological time is from new to old. It is generally consistent with the pre-stagnate sequence characteristics

of DGB landslide, indicating that although the scale of the landslide is huge, the sliding distance is not large, and the degree of disintegration of the accumulation is not high [33].

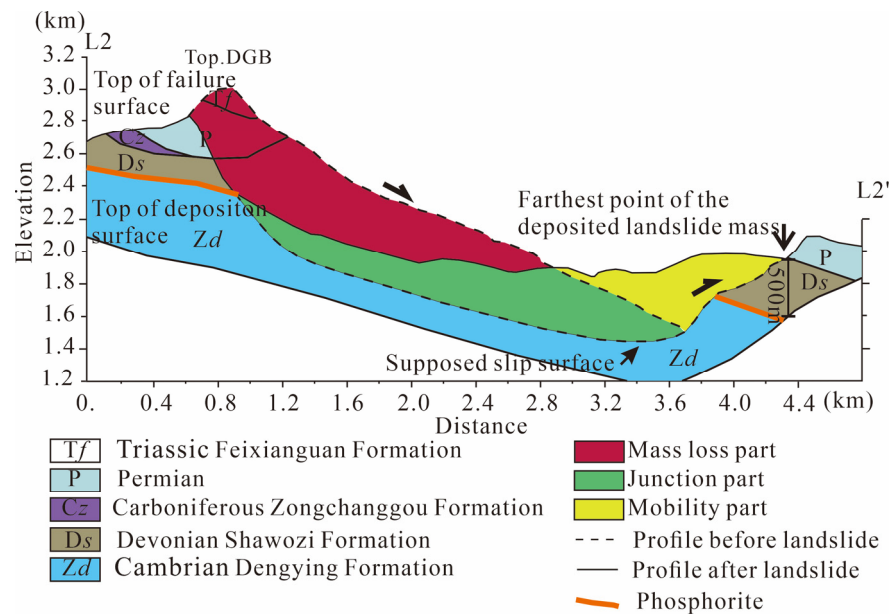


Figure 1. Geological profile of the DGB landslide.

2.2. Methods

The framework for studying the influence of vertical seismic acceleration on bedding fault-constrained landslide triggering under an inertial frame of reference is shown in Figure 2. This flowchart shows the beginning of the research with two parts: data and research object. The vertical seismic acceleration and  $c, \phi$  are used for computing the permanent displacement by Newmark method. Then,  $D/D^*$ , the effect of the inertia force and vertical acceleration, are analyzed to reverse the variation in permanent displacement, and the impact of internal friction angle ( $\phi$ ) and cohesion ( $c$ ) on the  $D/D^*$ .

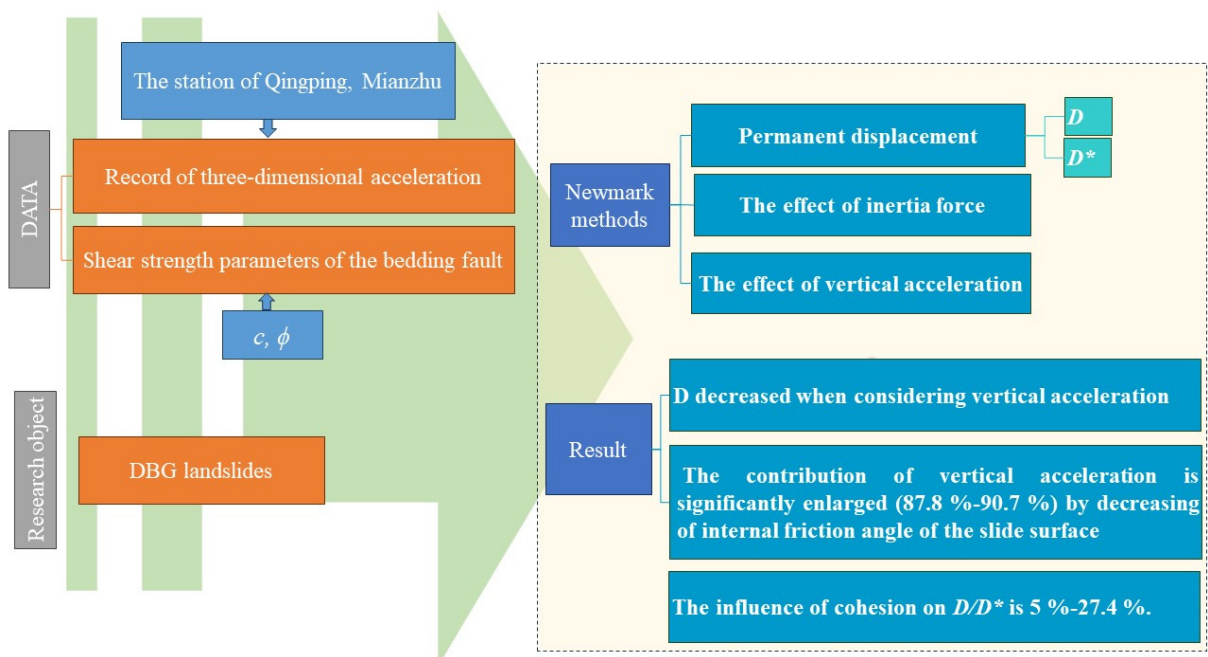


Figure 2. The framework of study.

### 2.2.1. The Permanent Displacement Analysis

The traditional seismic stability analysis of rock slope adopts the quasi-static method, which assumes that the seismic force is a constant force continuously applied in one direction, so only the peak ground acceleration (PGA) is considered. However, the seismic wave features such as type, frequency and duration are ignored, and the permanent displacement of the slope during an earthquake is not revealed. Newmark (1965) proposed the displacement analysis method based on the limited equilibrium theory of infinite slopes, which concluded that the permanent displacement of a sliding mass was caused by the displacement accumulation after instantaneous failure along the most dangerous sliding surface under seismic loading. The obtainment of the permanent displacement is divided into two steps: (1) The pseudo-static method is used to determine the critical acceleration of the potential sliding mass. When the acceleration at the most dangerous sliding surface exceeds the critical acceleration, the block slides along the failure surface. (2) The difference between the earthquake acceleration and the critical acceleration is quadratically integrated over time to obtain the permanent displacement (Figure 3). The calculation formula is as follows:

$$a_c = (F_s - 1)g \sin \delta \tag{1}$$

$$D = \iint_0^t [a_{(t)} - a_c g] dt^2 \tag{2}$$

where  $a_c$  is the critical acceleration,  $D$  is the permanent displacement,  $F_s$  is the pre-earthquake stability factor,  $g$  is the gravity acceleration (taken as  $9.8 \text{ m/s}^2$ ),  $\delta$  is the inclination of sliding surface,  $t$  is the time and  $a_{(t)}$  is the earthquake acceleration.

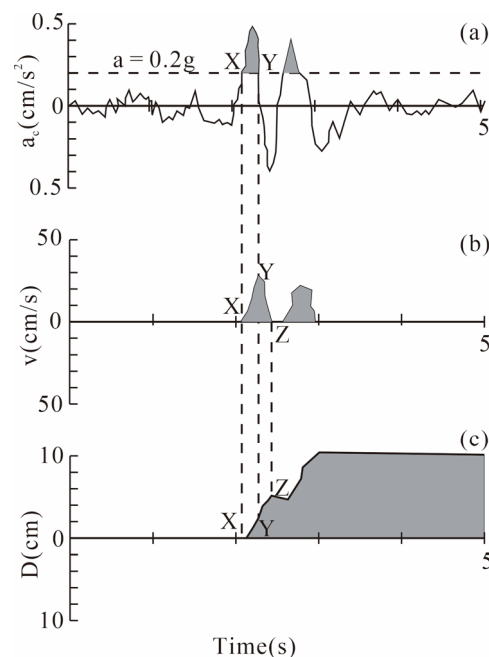


**Figure 3.** Schematic diagram of the Newmark method, (a) acceleration versus time, (b) velocity versus time and (c) displacement versus time [34].

The basic assumptions of the traditional Newmark method include the following:

- ① the sliding block is rigid, such as granite, dolomites, limestone and sandstone. They will have a cataclastic texture under the forces [35,36].
- ② The sliding block is displaced only when the seismic acceleration exceeds the critical acceleration.
- ③ The static and dynamic strength of the sliding surface is the same and fixed (without considering the deterioration).
- ④ Only the horizontal seismic force is considered (without considering the vertical seismic force).
- ⑤ The inertia force is not considered.

The sliding block is subjected to fixed sliding force and resistance force on the sliding surface when no earthquake occurs and remains in static equilibrium (Figure 4). The safety factor ( $F_s$ ) of the sliding block is defined as follows:

$$F_s = (\mu_s mg \cos \delta + cA) / (mg \sin \delta) \tag{3}$$

where  $m$  is the mass of the sliding block,  $g$  is the gravity acceleration (taken as  $9.8 \text{ m/s}^2$ ),  $\delta$  is the inclination of the sliding surface,  $\mu_s$  is the static friction coefficient,  $c$  is the cohesion and  $A$  is the sliding surface area.

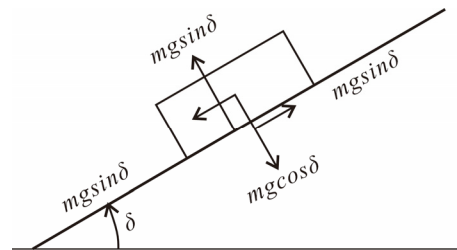


Figure 4. Force model of the sliding block in critical equilibrium before the earthquake [16].

During an earthquake, the critical equilibrium conditions of the sliding block are changed by ground vibration. The stability of the slider is controlled by the weight, the friction of the sliding surface and the acceleration in different directions. The seismic force acting on the slider can be decomposed perpendicular to the sliding surface ( $a_n$ ), parallel to the sliding surface along the inclination ( $a_d$ ) or parallel to the sliding surface along the direction ( $a_s$ ). They can be obtained by recording the east–west acceleration ( $a_E$ ), north–south acceleration ( $a_N$ ) and vertical acceleration ( $a_V$ ). The horizontal accelerations  $a_E$  and  $a_N$  are synthesized as acceleration  $a_s$  along the sliding direction, and then,  $a_s$  and  $a_V$  are synthesized as accelerations along the sliding direction  $a_d$  and vertical sliding direction  $a_n$ . The formula is as follows (Figure 5) [37]:

$$a_d = a_E \cos \delta \cos \varphi_s - a_N \cos \delta \sin \varphi_s - a_V \sin \delta \tag{4}$$

$$a_s = a_E \sin \varphi_s - a_N \cos \varphi_s \tag{5}$$

$$a_n = a_E \sin \delta \cos \varphi_s - a_N \sin \delta \sin \varphi_s + a_V \sin \delta \tag{6}$$

The slider generates inertial force with the ground movement, if not, consider inertia, and the slider and ground acceleration directions are the same when ground acceleration decreases or moves in the opposite direction (Figure 6). However, the slider and ground acceleration directions are opposite when considering inertia (Figure 7). The inertia force drives the slider movement, which helps produce displacement between the slider and the ground. The safety coefficients of the slider with and without considering the inertia force are as follows:

$$F_s = \left[ \mu_s (g \cos \delta + a_n) + \frac{cA}{m} \right] / (g \sin \delta - a_d) \tag{7}$$

$$F_s^* = \left[ \mu_s (g \cos \delta + a_n) + \frac{cA}{m} \right] / (g \sin \delta + a_d) \tag{8}$$

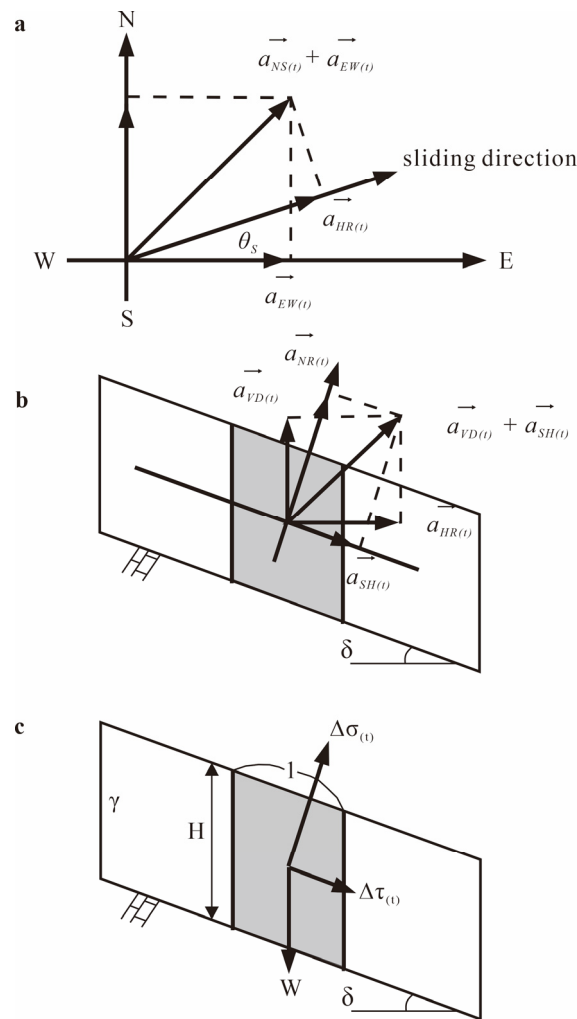


**Figure 5.** Schematic diagram of force decomposition on the potential sliding surface, (a) projection of horizontal acceleration along the cross-sectional direction, (b) projection of horizontal and vertical accelerations along the vertical and downslope directions, (c) seismic loading on the potential sliding surface [38].

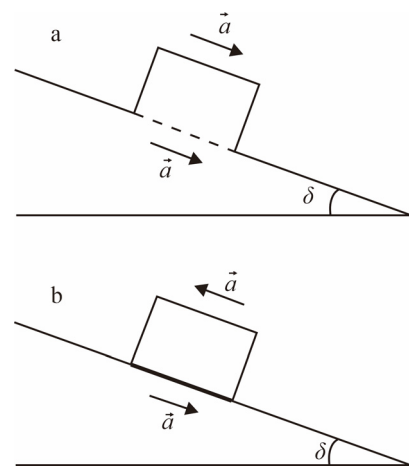


**Figure 6.** Schematic diagram of the acceleration direction of the slider and the base considering the non-inertia (a) and inertia forces (b) [39].

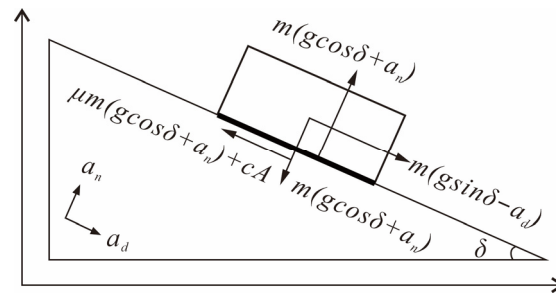


**Figure 7.** Force model of the critical equilibrium state of the slider during the earthquake (considering inertial force) (Huang et al., 2001) [16].

As defined by Newmark, the slider is stable when the sliding force is less than the resistance force, i.e.,  $F_s > 1$ . When  $F_s < 1$ , the slider will be destabilized along the sliding surface. Assuming that the slider is rigid, the acceleration along the sliding surface is calculated by the three directional acceleration components. The calculation formulas of acceleration with or without considering inertia force are as follows:

$$S = (g \sin \delta - a_d) - [\mu_s(g \cos \delta + a_n) + cA/m] \tag{9}$$

$$S^* = (g \sin \delta + a_d) - [\mu_s(g \cos \delta + a_n) + cA/m] \tag{10}$$

When  $S(S^*) < 0$ , the slider is at rest, and when  $S(S^*) > 0$ , the slider moves. According to Wilson and Keefer [40],  $S(S^*)$  is used instead  $[a_{(t)} - a_c g]$  in Equation (2) to obtain the permanent displacement induced by the earthquake.

The DGB landslide was generalized to a wedge-shaped slider of about 400 m height, 600 m width and 2200 m length (Figure 8). The orientation of the rock strata is N88°W/NE∠32°, and the apparent dip angle is calculated to be 17°. The landslide is primarily composed of carbonate rock, with the sliding plane being dominated by rigid dolomite, a type of hard rock. The downward acceleration and permanent displacement calculated by considering and ignoring vertical acceleration are  $S, S1, D$  and  $D1$ , respectively. Under the ignored inertial frame reference, the downward acceleration and permanent displacement calculated by considering and ignoring vertical acceleration are  $S^*, S1^*, D^*$  and  $D1^*$ , respectively.

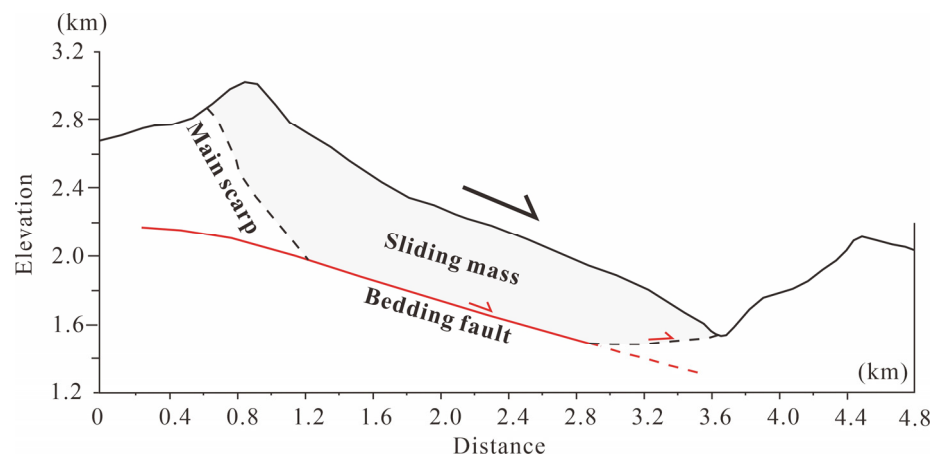


**Figure 8.** Block model of the DGB landslide.

2.2.2. Description of Three-Dimensional Acceleration

The distance between the DGB landslide and the epicenter of the Wenchuan earthquake is 85 km. The nearest seismic station to the DGB landslide is the Qingping station, whose seismic records are shown in Figure 9. The N-S, E-W and vertical acceleration peaks

are 0.803 g, −0.824 g and 0.623 g, respectively. The arrival time of the mainshock is about 25 s, and the duration time of the mainshock is about 25–60 s. The Newmark calculation is carried out using the acceleration data of Qingping station.

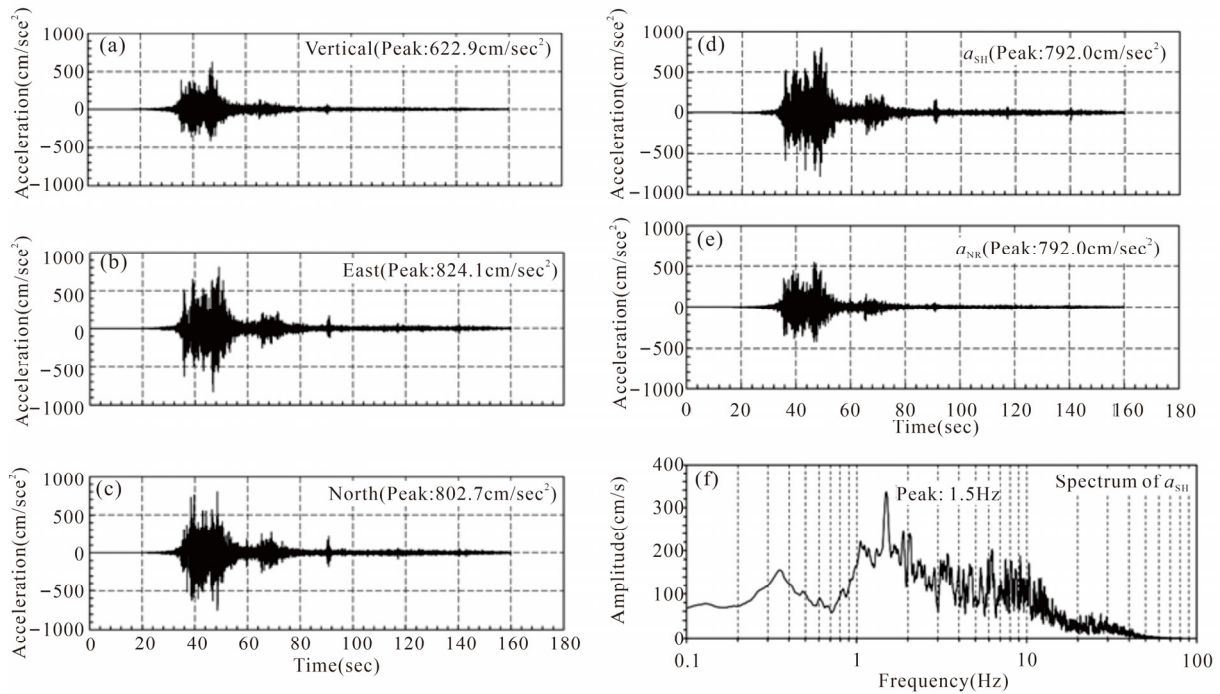


**Figure 9.** Seismic records from the Qingping seismic monitoring station during the Wenchuan earthquake, (a–c) accelerations in vertical (UD), east–west (EW), and north–south (NS) directions, respectively; (d,e) referred down-dip acceleration  $a_{SH}$  (downward positive) and normal acceleration  $a_{NR}$  (upward positive) along the sliding surface, respectively; (f) the frequency spectrum of  $a_{SH}$ .

The occurrence of an earthquake releases a lot of energy. We use the method proposed by Trifunac [41] to estimate the seismic energy of Wenchuan seismic wave passing through the sliding surface of the DGB landslide:

$$E_s = \left[ \frac{\rho A \alpha}{2\pi} \int_0^\infty \left( \frac{F(\omega)}{\omega} \right)^2 d\omega \right] \quad (11)$$

where  $F(\omega)$  is the Fourier amplitude spectrum of seismic acceleration along the sliding surface (cm/s),  $A$  is the sliding surface area ( $m^2$ ),  $\alpha$  is the shear wave velocity (m/s),  $\alpha = 1 \times 10^3$  m/s, and  $\rho$  is the density ( $kg/m^3$ ). The calculation results are shown in Figure 10. After the start of the earthquake, the initial energy growth is slow, and the energy increases rapidly in the period of 30–50 s. The energy release reaches 49.8% of the total energy in just 20 s. The energy growth slows down after 50 s and gradually approaches the final value after 120 s. The maximum energy release rate was about 45 s.

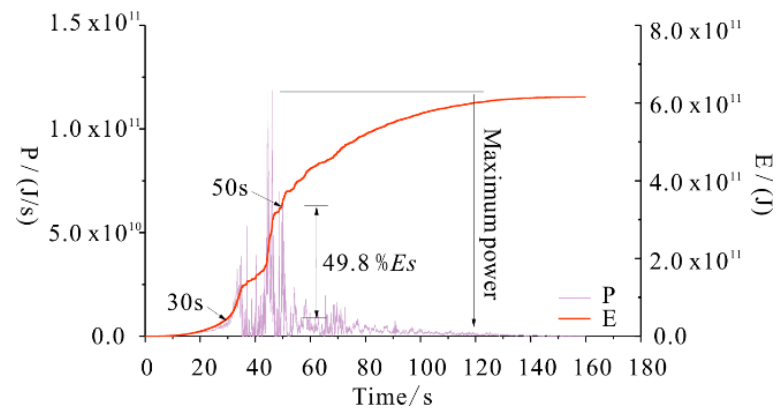


Figure 10. Energy analysis of Qingping seismic wave.

### 2.2.3. Shear Strength Parameters of the Bedding Fault

Previously, a large number of tests have been conducted to obtain the mechanical parameters of the sliding surface material, and these tests mainly include direct shear test, medium shear test, on-site large shear test, vane shear test, etc. The test results are shown in Figure 11. Among all the obtained test data, cohesion ( $c$ ) has a maximum value of 660 kPa and a minimum value of 20 kPa. The internal friction angle ( $\phi$ ) has a maximum value of  $41^\circ$  and a minimum value of  $17^\circ$ . The average values of  $c$  and  $\phi$  are 340 kPa and  $29^\circ$ , respectively. However, it is noted that all these tests are small displacement shear and do not include test results about velocity weakening, displacement weakening, liquefaction, melting, etc. [42–46]. In this study, we mainly analyze the initiation process of the DGB landslide under strong earthquakes, and the small displacement is generated in the process. Therefore, it can be reasonably assumed that the material strength weakening associated with long-distance shear is still not generated, and ignoring the strength weakening parameters has less influence on the calculation result.

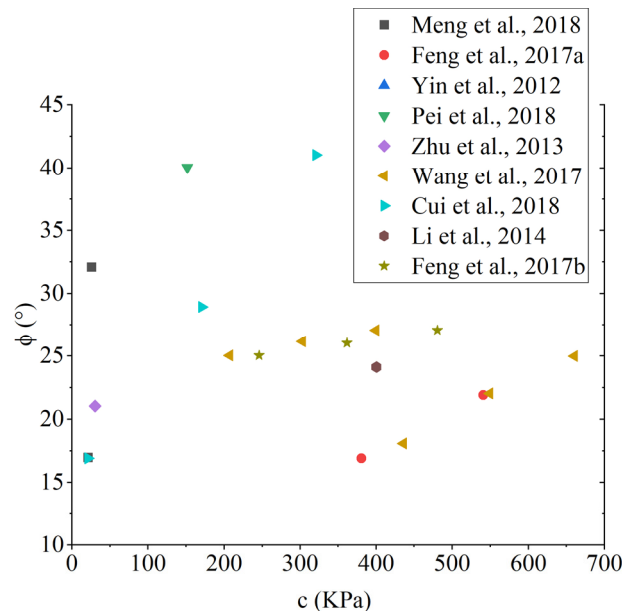


Figure 11. Statistics of shear strength parameters of rock masses in the slide zone of DGB landslide [47–55].

## 3. Results

### 3.1. Permanent Displacement

The  $F_s$  of the DGB landslide obtained by Equation (3) is about 1.9 (greater than 1), indicating that the DGB landslide was in a stable state before the earthquake, which

is consistent with the conclusion of the static analysis of the rigid block by Dong et al. (2017) [18]. Furthermore, we obtain the critical acceleration of the DGB landslide through Equation (1), which is 0.27 g (263.62 cm/s<sup>2</sup>). As shown in Figure 12, the peak value of  $S$  is significantly larger than the peak value of  $S_1$ , proving that the vertical acceleration increases the permanent displacement of the slider. In addition, the peak value of  $S^*$  (−994.8 cm/s<sup>2</sup>) is only slightly larger than that of  $S_1^*$  (−983.4 cm/s<sup>2</sup>). The permanent displacement that is influenced by the vertical acceleration and the inertial force is significantly larger than in the other three cases (i.e., only no vertical acceleration, only no inertial force, no vertical acceleration and inertial force).

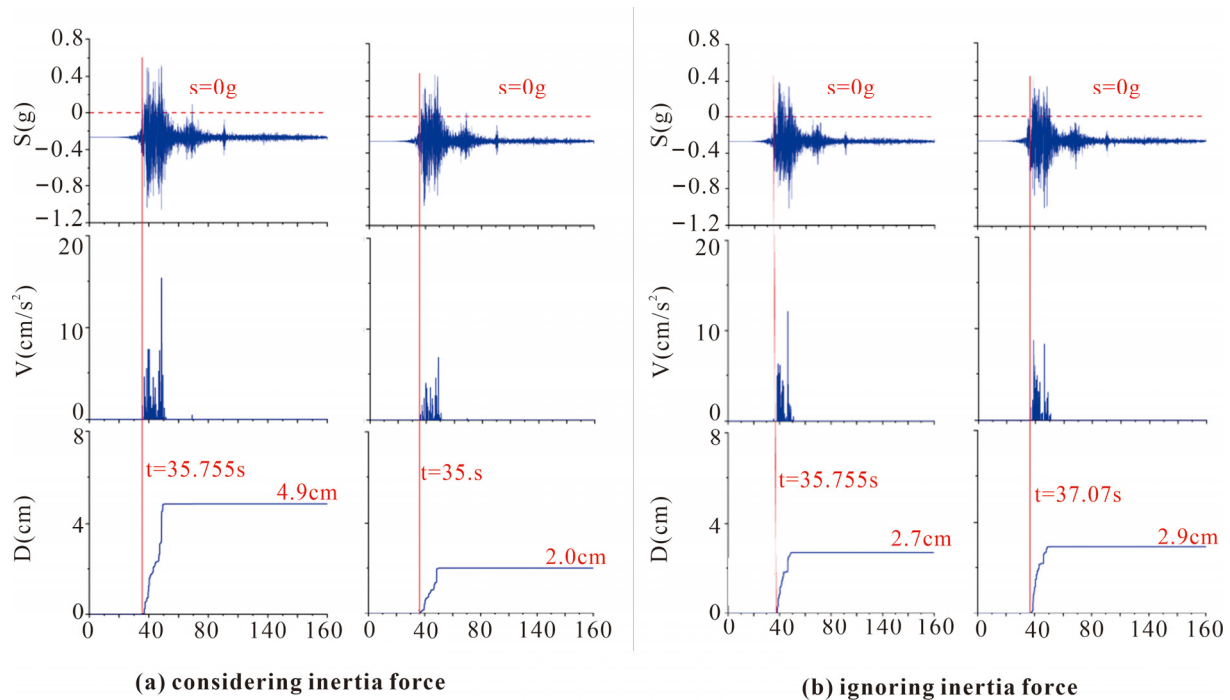


**Figure 12.** Permanent displacement of the slider.

To reveal the effect of the cohesion and internal friction angle on the stability coefficients of the DGB landslide before the earthquake, the cohesion was taken from 0 to 700, with 8 values at a spacing of 100, and the internal friction angle ( $\phi$ ) comprised 16 values from 10 to 40° at a spacing of 2°. As shown in Figure 13, the  $F_s < 1$  of the DGB landslide was obtained by some of the above parameters. We removed the parameters that made  $F_s < 1$ . The selection of the internal friction angle ( $\phi$ ) ranged from 14° to 40°.

Figure 14 shows the variation in the permanent displacement with the internal friction angle for the determined cohesion. When  $\phi < 18^\circ$ , the permanent displacement is 100~700 cm. When  $\phi$  is 18~26°, the permanent displacement is 100~10 cm. When  $\phi$  is 26~30°, the permanent displacement decreases to 5~10 cm. When  $\phi > 34^\circ$ , the permanent displacement is less than 1 cm. Figure 15 shows the variation in the permanent displacement with a cohesive determined internal friction angle. Compared with Figure 14, the permanent displacement decreases linearly with increasing cohesion, but the decrease rate is smaller. The effect of cohesion on the permanent displacement is slight.

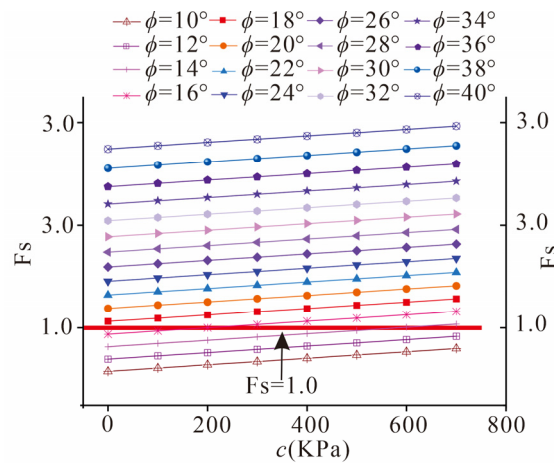


Figure 13. Effect of cohesion on  $F_s$  before earthquake.

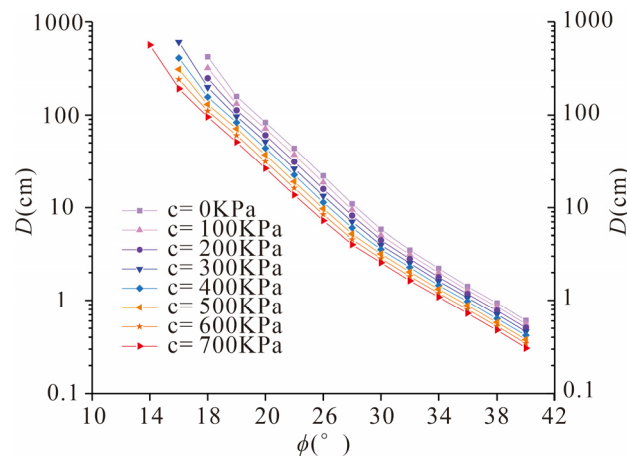


Figure 14. The variation in the permanent displacement with the internal friction angle.

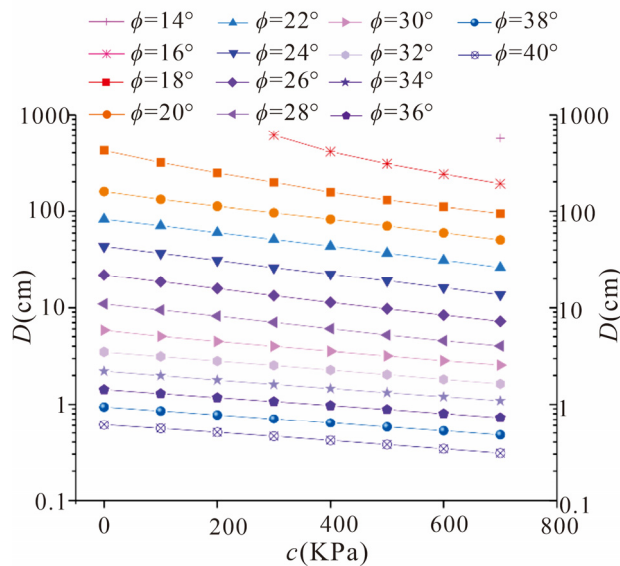
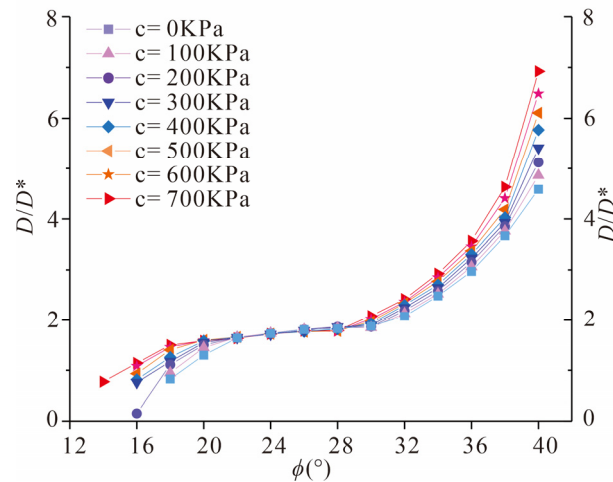


Figure 15. The variation in the permanent displacement with cohesion.

### 3.2. The Effect of Inertia Force

The permanent displacements under the inertial reference system ( $D$ ) and non-inertial reference system ( $D^*$ ) are calculated, respectively. Figures 16 and 17 show the displacement

ratios ( $D/D^*$ ) under different cohesions and internal friction angles, respectively. When the cohesion is certain, the  $D/D^*$  increases nonlinearly with an increasing internal friction angle. When  $\phi > 18^\circ$ , the  $D/D^*$  is greater than 1, and the maximum  $D/D^*$  reaches 7. When  $\phi < 22^\circ$ , the  $D/D^*$  increases in an upward convex pattern with an increasing internal friction angle. When the internal friction angle is  $22^\circ \sim 28^\circ$ , the increasing trend of  $D/D^*$  is not obvious. The  $D/D^*$  increases linearly with increasing cohesion. When the internal friction angle is certain, the change in cohesion has less influence on the  $D/D^*$ . When the internal friction angle is greater than  $30^\circ$ , the  $D/D^*$  is 2~7.



**Figure 16.** The relationship between the permanent displacement ratio and internal friction angle under different cohesions.

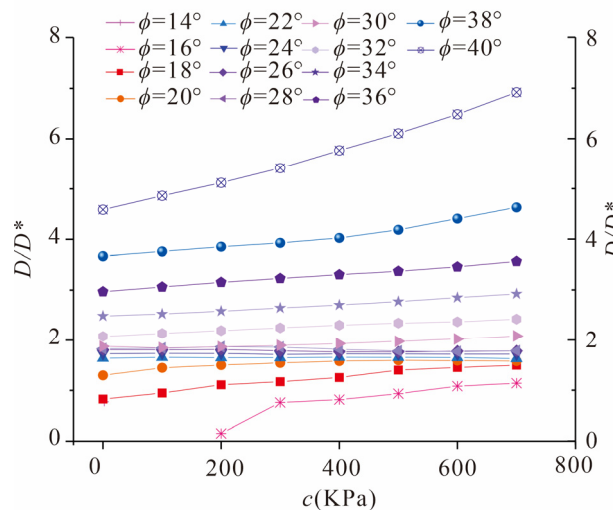


**Figure 17.** The relationship between the permanent displacement ratio and cohesion under different internal friction angles.

### 3.3. The Effect of Vertical Acceleration

The permanent displacements when considering vertical acceleration ( $D$ ) and ignoring vertical acceleration ( $D1$ ) are calculated, respectively. Figures 18 and 19 show the  $D/D1$  under different cohesions and internal friction angles, respectively. As shown in Figure 18, the  $D/D1$  increases rapidly with an increasing internal friction angle, and the maximum  $D/D1$  is 13. In addition, at a small internal friction angle, the cohesion has a small effect on the  $D/D1$ , and the minimum  $D/D1$  is greater than 1. As the internal friction angle increases, the influence of cohesion on the  $D/D1$  increases, which shows that the  $D/D1$  increases with increasing cohesion. From Figure 19, at smaller internal friction angles ( $14^\circ \sim 24^\circ$ ), the  $D/D1$

does not change significantly with increasing cohesion. When the internal friction angle is greater than  $24^\circ$ , the  $D/D1$  increases linearly with increasing cohesion, especially when the internal friction angle reaches  $40^\circ$ , at which point the increasing trend is more significant.

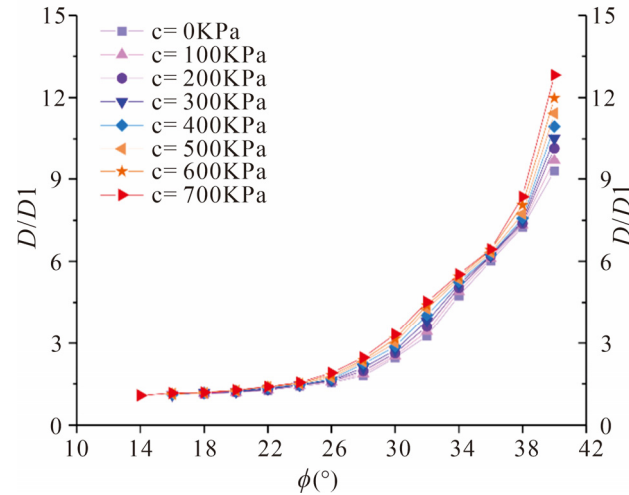


Figure 18. The relationship between the  $D/D1$  and internal friction angle under different cohesions.

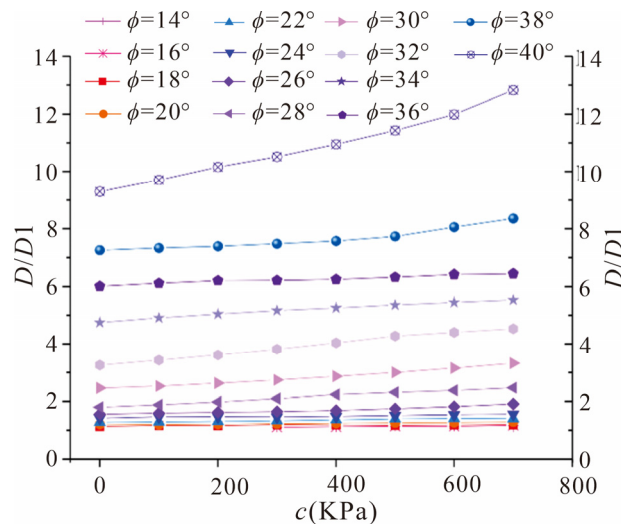


Figure 19. The relationship between the  $D/D1$  and cohesion under different internal friction angles.

#### 4. Discussion

Under the low shear strength parameters of the sliding surface, whether there is vertical acceleration or not, a small earthquake can produce a large permanent displacement. In this process, the contribution of vertical acceleration to the permanent displacement is not obvious. Upon analysis, it appears that this phenomenon can be attributed to the sliding surface angle being less than  $45^\circ$ . So, the vertical acceleration principal component lines up with the direction of the vertical sliding surface and affects the friction force by changing the normal stress of the slider. This will increase the permanent displacement of the landslide. Therefore, when the shear strength decreases, the impact of the vertical acceleration becomes less obvious. Although the permanent displacement decreases as the shear strength of the slide surface increases, the proportion of the permanent displacement caused by the vertical acceleration increases. For higher shear strength, the contribution of vertical acceleration to permanent displacement can cause initial displacement and contribute to the generation of a post-earthquake landslide.

As shown in Figure 20, considering the vertical acceleration, when the internal friction angle is  $18^\circ$ , the velocity pulse segment is in the range of 35 to 50 s, and the permanent displacement generated in this period accounts for 85.7% of the total permanent displacement. As the internal friction angle increases to  $40^\circ$ , the incremental percentage of permanent displacement increases from 86.3% to 95.3%. When the cohesion varies from 100 to 700 kPa, the velocity and permanent displacement response had the same pattern as that at  $c = 0$  kPa. When neglecting the vertical acceleration, the permanent displacement decreases, and the initial displacement generation time and rapid accumulation stage did not change for the same shear strength parameters. We speculate that the DGB landslide may have been triggered at the beginning of the earthquake (30–50 s). The occurrence time of the maximum accumulation rate of permanent displacement during the earthquake is mainly influenced by the period of concentrated release of seismic energy.

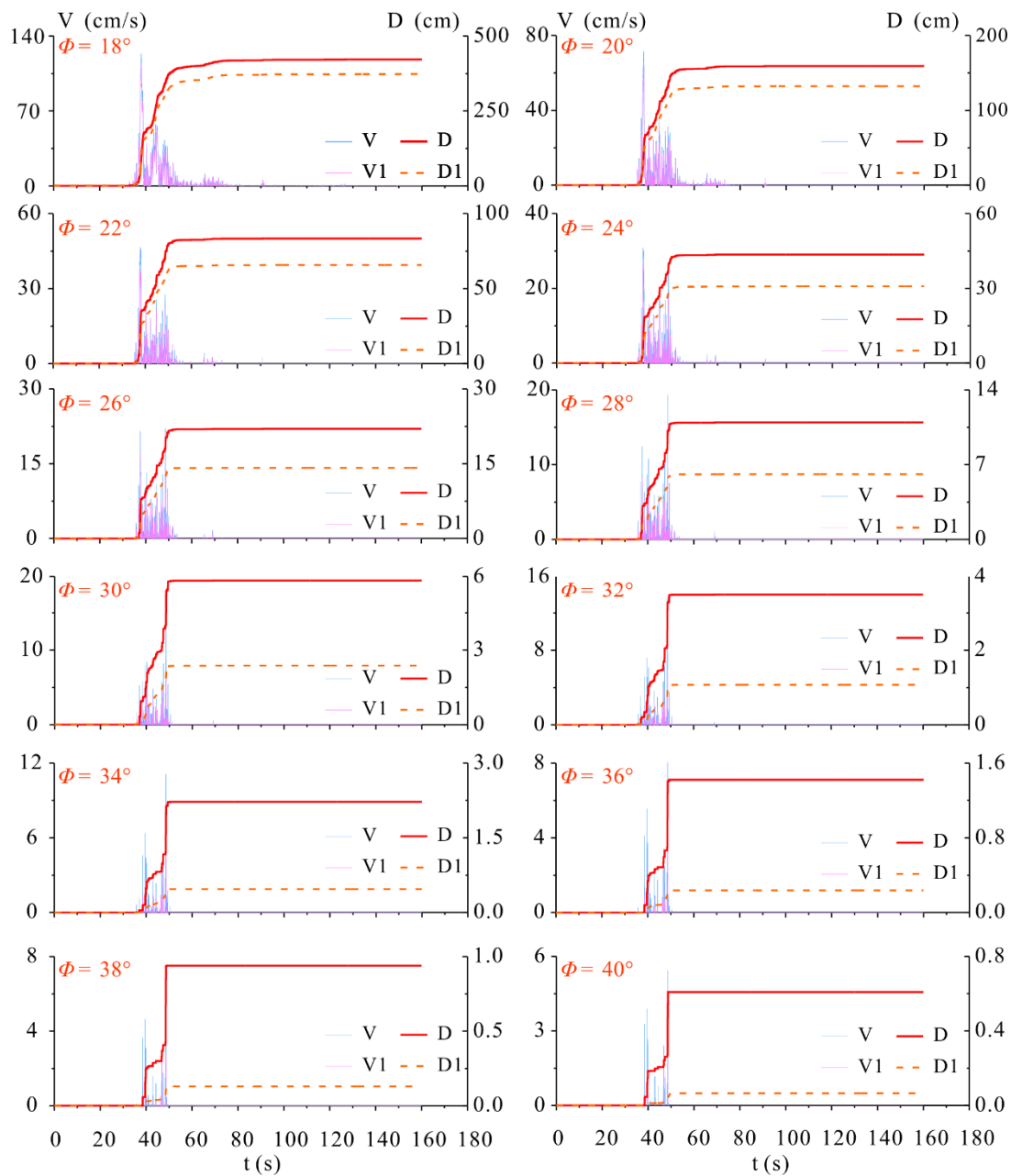


Figure 20. Velocity and displacement versus time under  $c = 0$  kPa.

## 5. Conclusions

In our study, differently to previous studies, the Newmark model that considers the vertical acceleration of earthquakes is used to reveal the initiation mechanism of the DGB landslide. By analyzing the change in permanent displacement, the following conclusions are obtained:

- (1) The vertical acceleration and horizontal inertia force significantly increased the permanent displacement of the DGB landslide and increased the possibility of landslide instability. The permanent displacement is 4.9 cm considering  $a_n$ , while it is just 2.0 cm without considering  $a_n$ .
- (2) Compared with the lower shear strength parameter of the sliding surface, the contributions of vertical acceleration and inertial force to the permanent displacement are more obvious when the shear strength parameter of the sliding surface is higher. When  $\phi > 18^\circ$ , the  $D/D^*$  is greater than 1, and the maximum  $D/D^*$  reaches 7. When  $\phi < 22^\circ$ , the  $D/D^*$  increases in an upward convex pattern with an increasing internal friction angle. When the internal friction angle is  $22^\circ \sim 28^\circ$ , the increasing trend of  $D/D^*$  is not obvious. The  $D/D^*$  increases linearly with increasing cohesion. When the internal friction angle is certain, the change in cohesion has less influence on the  $D/D^*$ . When the internal friction angle is greater than  $30^\circ$ , the  $D/D^*$  is 2~7;
- (3) The contribution of vertical acceleration is significantly enlarged (87.8–90.7%) by the decreasing of the internal friction angle of the slide surface, while it is less influenced (5–27.4%) by the cohesion.
- (4) The fast accumulation event of permanent displacement is triggered in the concentration stage of the seismic energy release, and 50% of the energy was released within 30–50 s in the DGB landslide area. It is assumed that the DGB landslide may have been triggered at 30–50 s due to 50% of the seismic energy being released in this time span.

**Author Contributions:** Conceptualization, G.X.; Methodology, Q.Y.; Software, T.J.; Validation, S.C.; Formal analysis, L.Z.; Investigation, Y.H.; Resources, H.L. All authors have read and agreed to the published version of the manuscript.

**Funding:** This study was financially sponsored by the Natural Science Foundation of Sichuan Province, China (Grants Nos. 2022NSFSC1121, 2022NSFSC1053 and 2023NSFSC0789).

**Institutional Review Board Statement:** Not applicable.

**Informed Consent Statement:** Not applicable.

**Data Availability Statement:** The data presented in this study are available on request from the corresponding author. The data are not publicly available due to privacy.

**Conflicts of Interest:** The authors declare no conflict of interest.

## Abbreviations

DGB landslide	Daguangbao landslide
Tf	Triassic Feixianguan Formation
P	Permian
Ds	Devonian Shawozi Formation
Zd	Cambrian Dengying Formation
PGA	Peak ground acceleration
UD	Accelerations in vertical directions
EW	Accelerations in east–west directions
NS	Accelerations in north–south directions

## References

1. Refice, A.; Capolongo, D. Probabilistic modeling of uncertainties in earthquake-induced landslide hazard assessment. *Comput. Geosci.* **2002**, *28*, 735–749. [[CrossRef](#)]

2. Ingles, J.; Darrozes, J.; Soula, J.C. Effects of the vertical component of ground shaking on earthquake-induced landslide displacements using generalized Newmark analysis. *Eng. Geol.* **2006**, *86*, 134–147. [[CrossRef](#)]
3. Shen, H.; Klapperich, H.; Abbas, S.M.; Ibrahim, A. Slope stability analysis based on the integration of GIS and numerical simulation. *Autom. Constr.* **2012**, *26*, 46–53. [[CrossRef](#)]
4. Jiao, Y.Y.; Wang, Z.H.; Wang, X.Z.; Adoko, A.C.; Yang, Z.X. Stability assessment of an ancient landslide crossed by two coal mine tunnels. *Eng. Geol.* **2013**, *159*, 36–44. [[CrossRef](#)]
5. Zhang, Z.; Wang, T.; Wu, S.; Tang, H.; Liang, C. Investigation of dormant landslides in earthquake conditions using a physical model. *Landslides* **2017**, *14*, 1181–1193. [[CrossRef](#)]
6. Belghali, M.; Saada, Z.; Garnier, D.; Maghous, S. Pseudo-static stability analysis of rock slopes reinforced by passive bolts using the generalized Hoek–Brown criterion. *J. Rock Mech. Geotech. Eng.* **2017**, *9*, 659–670. [[CrossRef](#)]
7. Gibson, M.D.; Wartman, J.P.; MacLaughlin, M.M.; Keefer, D.K. Pseudo-static failure modes and yield accelerations in rock slopes. *Int. J. Rock Mech. Min. Sci.* **2018**, *102*, 1–14. [[CrossRef](#)]
8. Fu, X.; Sheng, Q.; Du, W.; Mei, H.; Chen, H.; Du, Y. Evaluation of dynamic stability and analysis of reinforcement measures of a landslide under seismic action: A case study on the Yanyangcun landslide. *Bull. Eng. Geol. Environ.* **2020**, *79*, 2847–2862. [[CrossRef](#)]
9. Rodríguez-Peces, M.J.; Román-Herrera, J.C.; Peláez, J.A.; Delgado, J.; Tsigé, M.; Missori, C.; Martino, S.; Garrido, J. Obtaining suitable logic-tree weights for probabilistic earthquake-induced landslide hazard analyses. *Eng. Geol.* **2020**, *275*, 105743. [[CrossRef](#)]
10. Cui, S.; Pei, X.; Jiang, Y.; Wang, G.; Fan, X.; Yang, Q.; Huang, R. Liquefaction within a bedding fault: Understanding the initiation and movement of the Daguangbao landslide triggered by the 2008 Wenchuan Earthquake (Ms = 8.0). *Eng. Geol.* **2021**, *295*, 106455. [[CrossRef](#)]
11. Shukha, R.; Baker, R. Design implications of the vertical pseudo-static coefficient in slope analysis. *Comput. Geotech.* **2008**, *35*, 86–96. [[CrossRef](#)]
12. Kontoe, S.; Pelecanos, L.; Potts, D. An important pitfall of pseudo-static finite element analysis. *Comput. Geotech.* **2013**, *48*, 41–50. [[CrossRef](#)]
13. Liu, C.; Le, T.; Shi, B.; Zhu, Y. Discussion on three major problems of engineering application of the particle discrete element method. *Chin. J. Rock Mech. Eng.* **2020**, *39*, 1142–1152. (In Chinese)
14. Newmark, N.M. Effects of earthquakes on dams and embankments. *Geotechnique* **1965**, *15*, 139–160. [[CrossRef](#)]
15. Makdisi, F.I.; Seed, H.B. Simplified procedure for estimating dam and embankment earthquake-induced deformations. *J. Geotech. Eng. Div.* **1978**, *104*, 849–867. [[CrossRef](#)]
16. Huang, C.C.; Lee, Y.H.; Liu, H.P.; Keefer, D.K.; Jibson, R.W. Influence of surface-normal ground acceleration on the initiation of the Jih-Feng-Erh-Shan landslide during the 1999 Chi-Chi, Taiwan, earthquake. *Bull. Seismol. Soc. Am.* **2001**, *91*, 953–958. [[CrossRef](#)]
17. Yuan, R.M.; Tang, C.L.; Deng, Q.H. Effect of the acceleration component normal to the sliding surface on earthquake-induced landslide triggering. *Landslides* **2015**, *12*, 335–344. [[CrossRef](#)]
18. Dong, J.J.; Tsao, C.C.; Yang, C.M.; Wu, W.J.; Lee, C.T.; Lin, M.L.; Zhang, W.F.; Pei, X.J.; Wang, G.H.; Huang, R.Q. The geometric characteristics and initiation mechanisms of the earthquake-triggered Daguangbao landslide. In *Geotechnical Hazards from Large Earthquakes and Heavy Rainfalls*; Springer: Tokyo, Japan, 2017; pp. 203–213.
19. Harrington, C.C.; Liel, A.B. Collapse assessment of moment frame buildings, considering vertical ground shaking. *Earthq. Eng. Struct. Dyn.* **2016**, *45*, 2475–2493. [[CrossRef](#)]
20. Zaker Esteghamati, M. A Holistic Review of GM/IM Selection Methods from a Structural Performance-Based Perspective. *Sustainability* **2022**, *14*, 12994. [[CrossRef](#)]
21. Bayraktar, A.; Hökelekli, E.; Halifeoğlu, F.M.; Mosallam, A.; Karadeniz, H. Vertical strong ground motion effects on seismic damage propagations of historical masonry rectangular minarets. *Eng. Fail. Anal.* **2018**, *91*, 115–128. [[CrossRef](#)]
22. Rinaldin, G.; Fasan, M.; Noé, S.; Amadio, C. The influence of earthquake vertical component on the seismic response of masonry structures. *Eng. Struct.* **2019**, *185*, 184–193. [[CrossRef](#)]
23. Chen, Z.Y.; Chen, W.; Zhang, W.; Lou, M.L. Effects of axial compression ratio of central columns on seismic performance of a multi-story underground structure. *Int. J. Comput. Methods* **2016**, *13*, 1641014. [[CrossRef](#)]
24. Li, W.; Chen, Q. Effect of vertical ground motions and overburden depth on the seismic responses of large underground structures. *Eng. Struct.* **2020**, *205*, 110073. [[CrossRef](#)]
25. Quaranta, G.; Angelucci, G.; Mollaioli, F. Near-fault earthquakes with pulse-like horizontal and vertical seismic ground motion components: Analysis and effects on elastomeric bearings. *Soil Dyn. Earthq. Eng.* **2022**, *160*, 107361. [[CrossRef](#)]
26. Godt, J.; Şener, B.; Verdin, K.; Wald, D.; Earle, P.; Harp, E.; Jibson, R. Rapid assessment of earthquake-induced landsliding. In *Proceedings of the First World Landslide Forum, Tokyo, Japan, 18–21 November 2008*.
27. Wang, X.Y.; Nie, G.Z.; Wang, S. Evaluation criteria of landslide hazards induced by Wenchuan earthquake using fuzzy mathematical method. *Rock Soil Mech.* **2011**, *32*, 403–410.
28. Ma, S.Y.; Xu, C.; Wang, T.; Liu, J.M. Application of two simplified Newmark models to the assessment of landslides triggered by the 2008 wenchuan earthquake. *Seismol. Geol.* **2019**, *41*, 774–788.
29. Chen, Y.; Gu, H.; Lu, Z. Variations of gravity before and after the Haicheng earthquake, 1975, and the Tangshan earthquake, 1976. *Phys. Earth Planet. Inter.* **1979**, *18*, 330–338. [[CrossRef](#)]

30. Chen, Y.; Wu, F.T. Lancang—Gengma earthquake: A preliminary report on the 6 November 1988, event and its aftershocks. *Eos Trans. Am. Geophys. Union* **1989**, *70*, 1527–1540. [[CrossRef](#)]
31. Cui, S.; Pei, X.; Huang, R. Effects of geological and tectonic characteristics on the earthquake-triggered Daguangbao landslide, China. *Landslides* **2018**, *15*, 649–667. [[CrossRef](#)]
32. Zhu, L.; Pei, X.; Cui, S.; Wang, S.; Zhang, X.; Liang, Y. On the initiation mechanism of the Daguangbao landslide triggered by the 2008 Wenchuan (Ms 7.9) earthquake. *Soil Dyn. Earthq. Eng.* **2020**, *137*, 106272.
33. Pei, X.; Zhu, L.; Cui, S.; Zhang, X.; Liang, Y.; Gao, H.; Zhang, Z. Liquefaction characteristics of interlayer dislocation zone of Daguangbao landslide and its start-up cause. *Rock Soil Mech.* **2019**, *40*, 1085–1096.
34. Jibson, R.W.; Harp, E.L.; Michael, J.A. A method for producing digital probabilistic seismic landslide hazard maps. *Eng. Geol.* **2000**, *58*, 271–289. [[CrossRef](#)]
35. Salih, N.; Mansurbeg, H.; Kolo, K.; Pr eat, A. Hydrothermal carbonate mineralization, calcretization, and microbial diagenesis associated with multiple sedimentary phases in the upper cretaceous bekhme formation, Kurdistan Region-Iraq. *Geosciences* **2019**, *9*, 459. [[CrossRef](#)]
36. Salih, N.; Mansurbeg, H.; Muchez, P.; Gerdes, A.; Pr eat, A. Hydrothermal fluids and cold meteoric waters along tectonic-controlled open spaces in upper cretaceous carbonate rocks, Ne-Iraq: Scanning data from in situ u-pb geochronology and microthermometry. *Water* **2021**, *13*, 3559. [[CrossRef](#)]
37. Wang, G.; Sassa, K.; Fukuoka, H. Seismic behavior of saturated sandy soils: Case study for the May 2003 Tsukidate landslide in Japan. In *Landslides*; Springer: Berlin/Heidelberg, Germany, 2005; pp. 157–164.
38. Wang, G.; Sassa, K. Seismic loading impacts on excess pore-water pressure maintain landslide triggered flowslides. *Earth Surf. Process. Landf.* **2009**, *34*, 232–241. [[CrossRef](#)]
39. Liao, C.J.; Lee, D.H.; Wu, J.H.; Lai, C.Z. A new ring-shear device for testing rocks under high normal stress and dynamic conditions. *Eng. Geol.* **2011**, *122*, 93–105. [[CrossRef](#)]
40. Wilson, R.C.; Keefer, D.K. Dynamic analysis of a slope failure from the 6 August 1979 Coyote Lake, California, earthquake. *Bull. Seismol. Soc. Am.* **1983**, *73*, 863–877. [[CrossRef](#)]
41. Trifunac, M.D. Energy of strong motion at earthquake source. *Soil Dyn. Earthq. Eng.* **2008**, *28*, 1–6. [[CrossRef](#)]
42. Wang, G.; Huang, R.; Chigira, M.; Wu, X.; Louren o, S.D. Landslide Amplification by Liquefaction of Runout-Path Material after the 2008 Wenchuan (M 8.0) Earthquake, China. *Earth Surf. Process. Landf.* **2013**, *38*, 265–274. [[CrossRef](#)]
43. Lucas, A.; Mangeney, A.; Ampuero, J.P. Frictional velocity-weakening in landslides on Earth and on other planetary bodies. *Nat. Commun.* **2014**, *5*, 3417. [[CrossRef](#)]
44. Liu, W.; He, S.; Li, X.; Xu, Q. Two-dimensional landslide dynamic simulation based on a velocity-weakening friction law. *Landslides* **2016**, *13*, 957–965. [[CrossRef](#)]
45. Hu, W.; Huang, R.; McSaveney, M.; Yao, L.; Xu, Q.; Feng, M.; Zhang, X. Superheated steam, hot CO<sub>2</sub> and dynamic recrystallization from frictional heat jointly lubricated a giant landslide: Field and experimental evidence. *Earth Planet. Sci. Lett.* **2019**, *510*, 85–93. [[CrossRef](#)]
46. Deng, Y.; Yan, S.; Scaringi, G.; Liu, W.; He, S. An empirical power density-based friction law and its implications for coherent landslide mobility. *Geophys. Res. Lett.* **2020**, *47*, e2020GL087581. [[CrossRef](#)]
47. Meng, X.; Pei, X.; Huang, R.; Cui, S.; Zhu, L.; Zhan, W. Shear behaviors of rock mass in the interlayer fault zone of Daguangbao landslide. *J. Eng. Geol.* **2018**, *26*, 309–318. (In Chinese)
48. Feng, W.; Wang, Q.; Zhang, G.; Liu, Z.; Yi, X. Improvement of Hoek-Brown criterion and application of landslide zone of cataclastic rock mass mechanical strength in evaluation of Daguangbao landslide. *Chin. J. Rock Mech. Eng.* **2017**, *36* (Suppl. S1), 335–342. (In Chinese)
49. Yin, Y.; Wang, M.; Li, B.; Feng, Z. Dynamic response characteristics of Daguangbao landslide triggered by Wenchuan earthquake. *Chin. J. Rock Mech. Eng.* **2012**, *31*, 1969–1982. (In Chinese)
50. Pei, X.; Cui, S.; Huang, R. A model of initiation of Daguangbao landslide: Dynamic dilation and water hammer in sliding zone during strong seismic shaking. *Chin. J. Rock Mech. Eng.* **2018**, *37*, 430–448. (In Chinese)
51. Zhu, L.; Wang, X. Physical modeling and numerical simulation of deformation and failure process of large rockslide in earthquake. *J. Eng. Geol.* **2013**, *21*, 228–235. (In Chinese)
52. Wang, Q. *Strength Characteristics of Sinian Dengying Formation in Bedding Shear Zone of Daguangbao Landslide*; Chengdu University of Technology: Chengdu, China, 2017. (In Chinese)
53. Cui, S.; Pei, X.; Huang, R. An initiation model of DGB landslide: Non-coordinated deformation inducing rock damage in sliding zone during strong seismic shaking. *Chin. J. Rock Mech. Eng.* **2019**, *38*, 237–253. (In Chinese)
54. Li, T.; Pei, X.; Huang, R. A study of motion features of the Daguangbao large-scale landslide induced by the Wenchuan Earthquake. *Hydrogeol. Eng. Geol.* **2014**, *41*, 122–127. (In Chinese)
55. Feng, W.; Yi, X.; Ge, H.; Wang, Q.; Liu, Z.; Zhang, G. In-situ borehole shear test on cataclastic rock mass of Daguangbao landslide. *Chin. J. Geotech. Eng.* **2017**, *39*, 1718–1723. (In Chinese)

**Disclaimer/Publisher’s Note:** The statements, opinions and data contained in all publications are solely those of the individual author(s) and contributor(s) and not of MDPI and/or the editor(s). MDPI and/or the editor(s) disclaim responsibility for any injury to people or property resulting from any ideas, methods, instructions or products referred to in the content.